

<https://doi.org/10.1038/s41612-024-00721-2>

Anthropogenic effects on tropical cyclones near Western Europe

Shuai Wang¹ ✉, Hiroyuki Murakami² & William Cooke²

There is less consensus on whether human activities have significantly altered tropical cyclone (TC) statistics, given the relatively short duration of reliable observed records. Understanding and projecting TC frequency change is more challenging in certain coastal regions with lower TC activity yet high exposure, such as Western Europe. Here, we show, with large-ensemble simulations, that the observed increase in TC frequency near Western Europe from 1966 to 2020 is likely linked to the anthropogenic aerosol effect. Under a future scenario featuring regionally controlled aerosol emissions and substantially increased greenhouse gas concentrations (Shared Socioeconomic Pathway 5-85), our simulations show a potential decrease in TC frequency near Western Europe by the end of the 21st century. These contrasting trends in historical and future TC frequencies are primarily due to the rise for 1966–2020 and potentially subsequent fall for 2030–2100 in TC genesis frequency in the North Atlantic. The response of large-scale environmental conditions to anthropogenic forcing is found to be crucial in explaining the historical and future changes in TC frequency near Western Europe.

While tropical cyclones (TCs) and Western Europe may seem unrelated, historical encounters have been documented^{1–3}. When such encounters do occur, they may have a high impact. This is attributed not only to the damaging wind, heavy precipitation, high storm surge and rapid population and economic growth in coastal regions, but also to the relatively limited experience in preparedness and public awareness in Western Europe regarding these extremely destructive weather systems with tropical origin. For example, Hurricane Debbie (1961) struck Ireland as one of the most severe storms to affect the region, resulting in 18 fatalities and widespread damage⁴.

Counterintuitively, climatological analysis suggests that TCs hitting Western Europe are not as rare as one might think. Approximately 10% of Atlantic TCs have made landfall in Europe in the past four decades⁵, i.e., about one European landfall per year. More than half of the storms reaching Europe from the Atlantic tropics retain a warm cyclone core, bringing extreme winds at landfall⁶. However, TCs entering the midlatitudes sometimes lose their warm-core structure via extratropical transition upon reaching Western Europe^{7–11}. Strictly speaking, these transitioned storms are no longer considered tropical systems. Nevertheless, to distinguish them from extratropical cyclones generated in the midlatitudes, this study still refers to a storm as a “tropical cyclone” when it originates in the tropical Atlantic, even after undergoing extratropical transition. Regardless the TC stage when reaching Europe, the consequence of a TC landfall in Western Europe could be more catastrophic than those caused by mid-latitude

cyclones, as the former are, on average, significantly more intense when they make landfall in Europe¹².

TC impacts are primarily associated with their hazards, such as strong winds, precipitation, and storm surge. Recent TC studies provide relatively high confidence that TC peak winds, precipitation and storm-surge-related flooding may increase with global warming^{13–16}. However, TC frequency (TCF), the number of TC occurrence over a given period and region, is one of the important TC metrics relevant to the overall hazard and risk. Despite its importance, TCF is arguably the least understood component under climate change, both globally and within individual ocean basins¹⁷. There are multiple reasons for this lack of understanding. First, it is extremely challenging to capture a comprehensive long-term trend in TCF using paleoclimate archive proxies¹⁸. Second, historical simulations with current-generation climate models do not always accurately represent the observed TCF¹⁹. Third, model simulations sometimes show inconsistent projections for TCF under global warming²⁰. More importantly, an accepted theory that can explain the global mean TCF and its temporal variations is still lacking¹⁷.

With the rapid development of high-performance computing, it is now possible to employ general circulation models with a relatively fine grid spacing to understand past and project potential future changes in TCF^{21,22}. In this study, we utilize a recently developed next-generation global modeling system known as Seamless System for Prediction and Earth System Research (SPEAR)²³. The SPEAR simulation suite can be considered as a unique global modeling system because it possesses the capability for TC

¹Department of Geography and Spatial Sciences, University of Delaware, Newark, DE, USA. ²National Oceanic and Atmospheric Administration/Geophysical Fluid Dynamics Laboratory, Princeton, NJ, USA. ✉e-mail: shwang@udel.edu

simulations while conducting numerical experiments to distinguish the effects of anthropogenic aerosols and greenhouse gases (GHGs) on weather extremes simultaneously. This work is a follow-up investigation of a recent study that focused on the changes in TCF within the tropics²⁴. Here we extend the previous analysis to examine the impact of TC activity at mid-latitudes. In this study, we employ this modeling system, together with TC best-track observations, to investigate the following question:

How has TCF changed and will it change near Western Europe, and why?

Results

The TC frequency, TCF, is calculated as the frequency of TC appearances in 5° × 5° grid boxes based on 6-h records. A tropical cyclonic system is referred to as a “TC” here as long as it reaches a peak wind speed above gale-force (34

knots), regardless of the stage of TC’s lifecycle. The analysis period was confined from 1966 – 2020, i.e., the current geostationary satellite era in the North Atlantic²⁵.

Observations

Our analysis begins with the examination of TCF using the TC best track data. Figure 1a shows an increase in mean TCF from the period of 1966–1993 to 1993–2020. Two clusters with statistical significance can be visually identified, one over the tropical Atlantic Ocean and the other near Western Europe (magenta box in Fig. 1a which will be identified specifically with further analysis later). Compared to that in the tropics, the TCF increase is relatively weaker near Western Europe. However, this increase can be as high as 200% relative to the climatological annual mean TCF there (Fig. 1b).

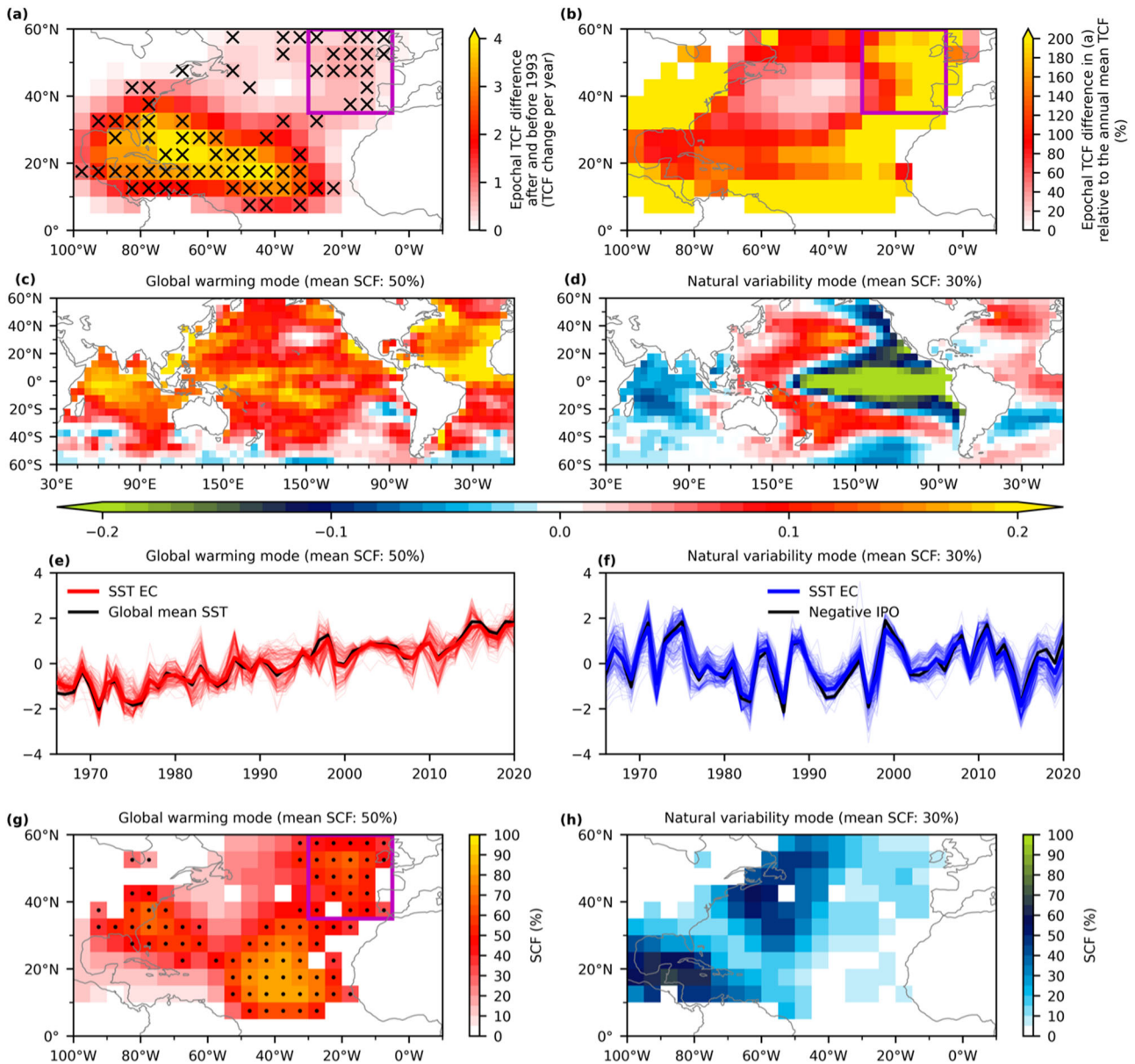


Fig. 1 | Analysis of observed TCF variations for 1966–2020. a Shifts in TCF before and after 1993, with black “x” marks indicating significant changes at a 90% confidence level, determined by a two-sided bootstrap test (see Methods). **b** Epochal TCF difference as shown in (a) divided by the annual mean TCF in each grid. **c–h** Analysis of regional SVD based on SST and TCF data. **c** A synthesis of the SVD mode that reflects the mean global SST change. **d** Similar to (c), but for the SVD mode related to the internal climate variability featured by the IPO pattern. **e** The

expansion coefficient (EC) for the global mean SST mode, overlaid with the global mean SST. **f** As in (e), but for the natural variability mode, overlaid with an inversed IPO index. **g** Squared covariance fraction (SCF) for the global mean SST mode (with SCF ≥ 50% marked by black dots). **h** As in (g), but for the natural variability mode. The magenta box in (a, b, g) highlights the region near Western Europe where the TCF increase is statistically significant in (a) and the global mean SST increase may dominate such TCF changes as shown in (g).

It is possible that these trends could be associated with the artificial changes in analysis technique and protocols to extract TCs in observations, specifically for the mid-latitude TCs for which they undergo extratropical transition. Supplementary Figure 1 shows that there is no discernible trend in the relative frequency of extratropical transition in the best track data, nor any notable tendency in the northernmost latitude where TCs have been recorded. This suggests that the observed increase in TCF near Western Europe may be associated with changes in the climate system itself, rather than being related to artificial changes in TC recording.

The singular value decomposition (SVD, see Methods) analysis was then employed to decompose the possible relationships between the change in TCF in the North Atlantic and the variations of the climate system through the global sea surface temperatures (SSTs)^{21,24}. The leading mode of the global SVD analysis effectively captures the scenarios of basin-wide TCF increase and global warming (Supplementary Fig. 2a–c), with the Expansion Coefficient (EC) showing the highest correlation with the global mean sea surface temperature (SST) increase (Supplementary Table 1). The second SVD mode closely resemble the Interdecadal Pacific Oscillation^{26,27} (IPO) setup (Supplementary Fig. 2d–f and Supplementary Table 1).

A regional SVD analysis²⁴ (see Methods) was performed to further target the TCF change near Western Europe. Different from a global SVD, a regional SVD utilizes the TCF information of each grid box and the global SST field (see Methods). The regional SVD analysis shows a consistent decomposition similar to that of the global SVD analysis, with the leading mode reflecting the mean increase in global SST and the second mode resembling the IPO configuration (Fig. 1c–f).

An advantage of regional SVD is that it allows us to identify if TCF changes for each grid box are highly correlated with global warming mode or IPO mode by comparing the squared covariance fraction (SCF) of the two modes. Figure 1g, h highlight the dominant role of the mean SST increase on the TCF increase in the deep Atlantic tropics, near the US east coast, and near Western Europe.

Based on this observational analysis, we can now identify an area near Western Europe (the magenta box in Fig. 1a and g), where we observe both a significant increase in TCF for 1966–2020 and the predominant influence of global mean sea surface warming (i.e., anthropogenic forcing) on the TCF change there. We do not directly analyze the number of landfalling TCs in Western Europe due to an insufficient sample size for statistical testing. However, this limitation can be addressed by analyzing the TCs within the magenta box in Fig. 1a. This box is small enough to assume that the wind field may intersect land boundaries in Western Europe, yet large enough to include enough TC samples for statistical testing.

One should note that this SVD analysis is purely statistical and may not perfectly separate the effects of anthropogenic climate change from natural variability from a physical perspective, particularly considering that the two factors—i.e., anthropogenic change and internal climate variability—might interact with each other. Nevertheless, this SVD analysis provides a convenient way to identify the region where anthropogenic change may significantly alter the TCF. The TCF change in the magenta box, as shown in Fig. 1 near Western Europe, is the focus of the following analysis.

Simulations

The extensive SPEAR simulations conducted under different climate forcings offer valuable opportunities to explore the reasons behind the historical increase in TCF near Western Europe and to understand the potential future changes. Here our focus is on the individual impacts of two anthropogenic forcings—specifically aerosols versus greenhouse gases (GHGs)—on the changes in TCF near Western Europe during two distinct periods: historically, from 1966–2020; and in the future, from 2030–2100. We employed three sets of large-ensemble simulations: (1) those including anthropogenic aerosol and GHG forcing covering 1966–2100 (referred to as *AllForc*), (2) those with only anthropogenic GHG forcing covering 1966–2020 (*AllForc_NoAE*), and (3) those with natural forcing only covering 1921–2100 (*NatForc*). Two Shared Socioeconomic Pathways (SSPs) are considered in future scenario simulations: SSP2-45 and SSP5-85. Next,

we investigate the TCF trend difference within multiple pairs of simulation suites to isolate the impacts of individual external forcings on TCF changes (see Methods for details).

We find an increase in TCF for 1966–2020 in simulations under the anthropogenic aerosol effect (Fig. 2a), but not with GHG or natural forcing for the same period (Fig. 2b, c). Combining the anthropogenic aerosol and GHG effects, an increase in TCF near Western Europe persists for 1966–2020 (Fig. 2d). The simulated TCF trend near Western Europe has comparable magnitudes as found in observations (Fig. 1). These results indicate that the increases in TCF are primarily owing to the anthropogenic aerosol changes with slight offset by GHG.

A previous study²² revealed that the TCF in North Atlantic may be mainly influenced by the aerosol emission in Europe and the US, rather than emissions from other regions worldwide. Some SSPs assume a future scenario characterized by well-controlled aerosol emissions in Europe and the US, but a substantially increased greenhouse gas concentration globally (Supplementary Fig. 3). When we employ such a scenario as external forcing in our simulations and compare to the results under natural forcing (i.e., *AllForc* minus *NatForc*), we project a reduction in the TCF near Western Europe for 2030–2100 under SSP2-45, mainly due to the anthropogenic GHG effect (Fig. 2e). This reduction becomes statistically significant in the future following SSP5-85 near Western Europe, again, primarily due to the anthropogenic GHG effect (Fig. 2f).

Next, we apply a Total Analysis to decompose the TCF change into contributions from TC genesis, TC track, and the nonlinear combination of the two (see Methods and Supplementary Fig. 4). The changes in genesis contribute considerably to both the increase in TCF near Western Europe under anthropogenic aerosol effect for 1966–2020, and the decrease under the GHG effect for the period 2030–2100 (Table 1). The track contribution is also an important factor for the TCF increase with aerosol forcing, but not under the GHG effect.

We then utilize the Origin Analysis (see Methods) to identify the key genesis areas where TCs originate and subsequently affect the TCF near Western Europe through direct genesis change and/or track change as they move toward Western Europe. Supplementary Figure 5a suggests that the TC genesis increase in the main development region (MDR; 10°–20°N, 60°–15°W) primarily contributes to the TCF increase near Western Europe for 1966–2020 under the aerosol effect, and conversely, the TC genesis reduction there contributes to the TCF reduction for 2030–2100 with GHG forcing (Supplementary Fig. 5d). Track change for TCs originating close to Africa also appears to play a secondly role in the TCF increase near Western Europe for the period 1966–2020 under the aerosol effect. With the strong control of genesis under both aerosol and GHG effects during the two periods, we next only focus on the genesis change.

TC genesis is largely controlled by the large-scale environmental conditions, and the Genesis Potential Index (GPI) serves as a useful proxy to understand this environmental control. A popular choice of GPI was proposed by Emanuel and Nolan²⁸ (hereafter the ENGPI), and a new GPI was also developed recently based on environmental dynamical factors²⁹ (hereafter DGPI). Comparing to the simulated tropical cyclone genesis frequency (TGF, Fig. 3a and d), DGPI can well reproduce the increase in genesis for the period 1966–2020 under the aerosol effect, and the subsequent decrease for 2030–2100 with GHG forcing. However, ENGPI fails to indicate the simulated TGF reduction in the future (Fig. 3f). Consequently, we exclusively utilize DGPI for the following analysis.

By breaking down the DGPI contributions from its four factors, it becomes evident that the reduction in vertical wind shear is the dominant factor contributing to the increase in TGF over the MDR for period 1966–2020 under the aerosol effect (Table 2 and Supplementary Fig. 6a–e). With the vertical wind shear further decomposed, the change in zonal shear is mainly responsible for the overall shear reduction (Supplementary Fig. 7b). This is mainly attributed to a weakening of subtropical jet over the MDR at 200 hPa (Supplementary Fig. 7d). It has been argued^{22,24,30–32} that the potential jet weakening in the past a few decades may be linked to a stronger mid-latitude low-tropospheric warming (Supplementary Fig. 8). This, in

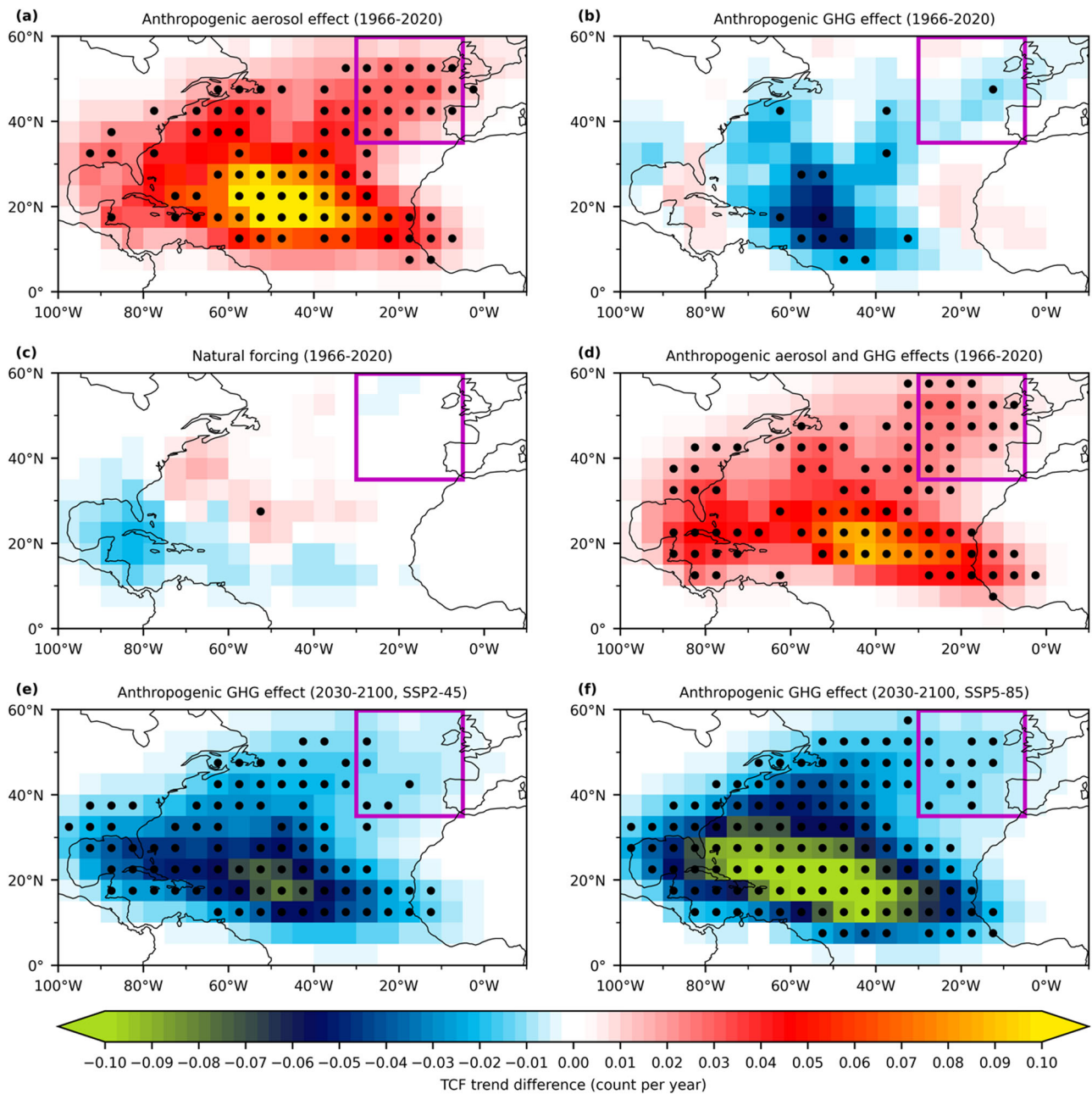


Fig. 2 | Ensemble mean TCF Trends under anthropogenic forcing. The trends are derived from ensemble mean annual TCF, forced by (a) anthropogenic aerosol effect (*AllForc* minus *AllForc_NoAE*), (b) anthropogenic greenhouse gases (*AllForc_NoAE* minus *NatForc*), (c) natural forcing (*NatForc* minus *CNTL*) and (d) the combined effects of anthropogenic aerosols and greenhouse gases (*AllForc* minus *NatForc*), for

the period 1966–2020. e As in (b), but for the period 2030–2100 under SSP2-45. f As in (b), but for the period 2030–2100 under SSP5-85. Black dots indicate locations where the average TCF trends between two sets of experiments show statistical differences at a 90% confidence level, as determined by a two-sided *t*-test. The magenta boxes correspond to that in Fig. 1, highlighting the region near Western Europe.

Table 1 | The contribution of genesis, track, and the nonlinear combination of the two to the simulated total TCF change near Western Europe

	Genesis contribution	Track contribution	Nonlinear contribution	Total contribution
Aerosol effect (1966–2020)	+50%	+39%	+11%	100%
GHG effect (2030–2100)	+107%	-16%	+9%	100%

The simulated TCF mean change is calculated in the magenta box as identified in Fig. 1a.

turn, perturbs and weakens the climatological subtropical jet through thermal wind adjustment.

For the period 2030–2100 with GHG forcing, the weakening of ascending motion over the MDR emerges as a leading factor (Table 1,

Supplementary Fig. 6f–j) contributing to the negative trend of DGPI. Further analysis reveals that the MDR region may experience a weaker SST increase under the GHG effect for 2030–2100, surrounded by much warmer SSTs in the mid-latitude North Atlantic, South Atlantic, and eastern

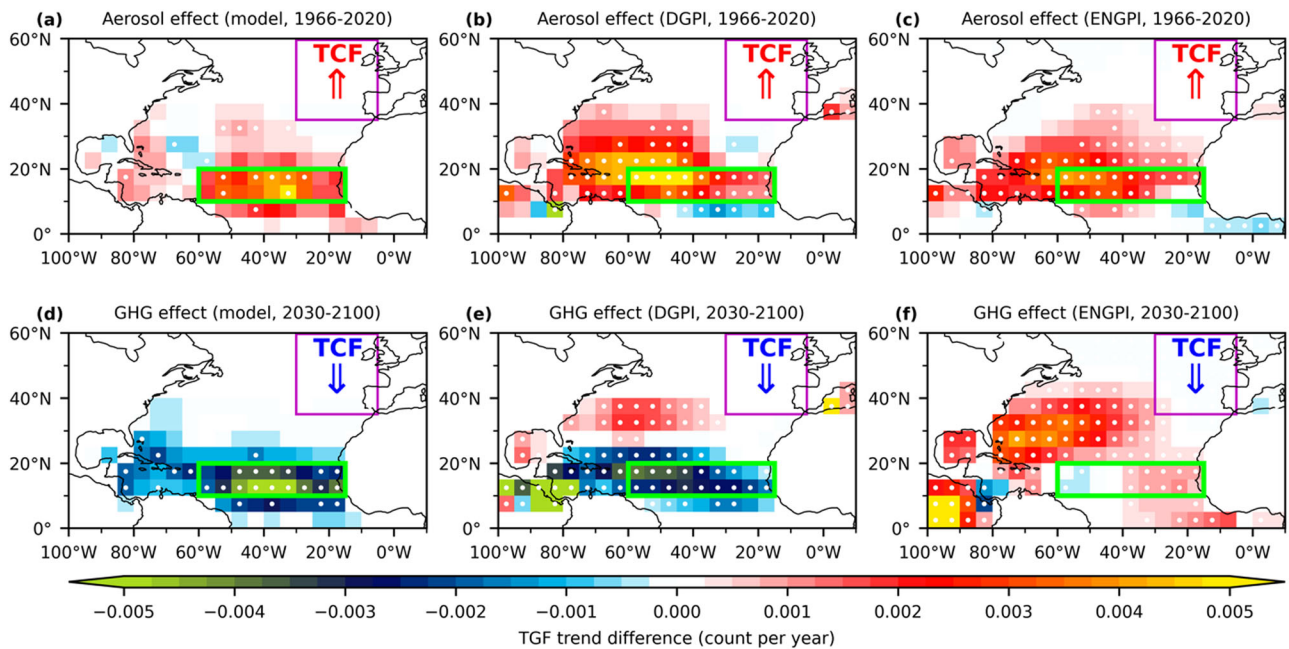


Fig. 3 | Tropical cyclone genesis (TGF) frequency trend. Trends of ensemble mean TGF in simulations under (a) anthropogenic aerosol effect (1966–2020) and (d) GHG effect (2030–2100), respectively, in a unit of genesis count per year. Trends of ensemble mean (b, e) DGPI and (c, f) ENGPI under (b, c) anthropogenic aerosol effect (1966–2020) and (e, f) GHG effect (2030–2100), respectively. White dots indicate locations where the trend is statistically significant at 90% confidence

intensity based on a two-sided *t*-test. Within the magenta box near Western Europe, the red font “TCF” and “↑” in (a–c) highlight the simulated increase in TCF under the aerosol effect for the period 1966–2020, as shown in Fig. 2a. Similarly, the blue font “TCF” and “↓” in (d–f) indicate the reduction in TCF as shown in Fig. 2f under the GHG effect for 2030–2100.

Table 2 | Decomposition of DGPI trend

	VORT	OMEGA	V-SHEAR	M-SHEAR	Total contribution
Aerosol effect (1966–2020)	17%	25%	44%	14%	100%
GHG effect (2030–2100)	7%	56%	-2%	39%	100%

The DGPI equation is linearized by taking the logarithm. The mean $\log(\text{DGPI} + 1)$ change in the main development region is broken down into the relative contribution (in a unit of %) of four terms related to the change of absolute vorticity (VORT), vertical motion (OMEGA), vertical wind shear (V-SHEAR), and meridional shear vorticity (M-SHEAR). A positive contribution of one term means the logarithm of the trend of this term shows the same sign as the mean $\log(\text{DGPI} + 1)$ trend difference.

equatorial Pacific (Supplementary Fig. 9a). Such an SST pattern creates a relatively “dry” region over the MDR with reduced convection (Supplementary Fig. 9b), resulting in a weakening of ascending motion there (Supplementary Fig. 9c).

TC hazard

The change in TCF is an essential factor influencing TC-related risk changes in coastal regions. However, to assess this, changes in other TC characteristics must also be considered. Under the combined effects of aerosols and GHGs, there is an initial increase (1966–2020) and then a subsequent decrease (2030–2100) in TCF near Western Europe in our simulations (Fig. 4a). However, there are no clear trends in TC intensity near Western Europe in observations or model simulations for both present-day and future (Fig. 4b). If the Accumulated Cyclone Energy (ACE, Bell et al., 2000), a measure combining TCF and TC intensity, is chosen to indicating the potential change in TC hazard, the associated risk near Western Europe have been increasing since 1966 and could drop in the future, primarily due to the changes in TCF in that region.

Discussion

Two kinds of temperature changes may be associated with the historical and future changes in TCF near Western Europe. First, for the increase in TCF for the period 1966–2020, it is the mid-latitude atmospheric warming that weakens the subtropical jet over the MDR region through thermal wind adjustment, subsequently reducing vertical wind shear. This, in turn, favors

TC genesis in the deep tropical Atlantic. Therefore, the reduction of aerosol emissions in Europe and the US in the past few decades may be the reason for the recent increase in TCF near Western Europe.

Second, concerning the decrease in TCF near Western Europe for period 2030–2100, the Atlantic MDR region exhibits a relatively weaker SST increase compared to the surrounding maritime regions under the GHG forcing, along with a substantially flattened aerosol emission curve in the western world. These factors lead to reduced convection and ascending motion over the MDR, subsequently suppressing TC genesis that in turn leads to a reduction in TCF near Western Europe.

In terms of TC hazard changes, the ACE near Western Europe may have increased for the period 1966–2020 but is expected to decrease for 2030–2100. This change in risk is primarily driven by the change in TCF since the mean TC intensity does not show any significant trend in simulations for both past and future. One should note that the TC precipitation-related hazard, which also changes under anthropogenic climate change, is not considered here. For example, a prior study³³ indicated that even with a potential decrease in the number of TCs making landfall over the eastern U.S. in the future, the intensity of TC extreme precipitation could be expected to rise, leading to an increase in TC hazard potential.

If we assume that the TCF near Western Europe tends to follow the mean change in the basin, most climate models projects a decrease in TCF in North Atlantic into the future¹⁶, which aligns with our simulations. However, there is still no consensus on the changes in TCF near Western Europe. Previous studies with prescribed SST distributions under global warming

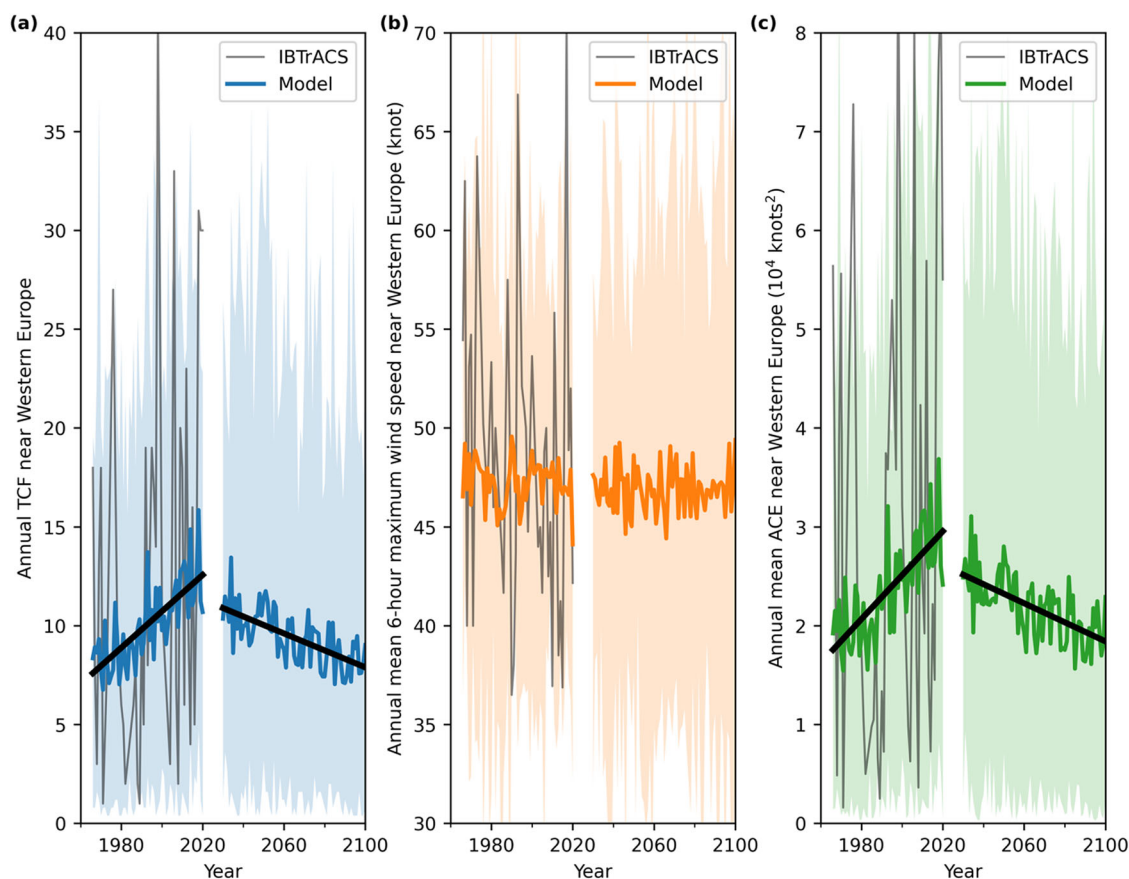


Fig. 4 | Observed and simulated TC changes in the past and projection into future. **a** Annual TCF near western Europe. The thin line shows the TCF change in HURDAT, taken as observation, for 1966–2020. The thick lines shown model ensemble mean change for 1966–2020 in *AllForc* and 2030–2100 under SSP5-85, respectively. The shading shows the range of all ensembles. **b** As in (a), but for the

annual mean maximum wind speed (knots) for the TCs near Western Europe (within the magenta box in Fig. 1a) based on the 6-h records. **c** As in (b), but for the annual mean accumulated cyclone energy (ACE, 10^4 knots²) for the TCs near Western Europe. If an ensemble trend shows statistically significant change at 5% level, a fitted thick black line is added for the period, as shown in (a) and (c).

have suggested the possibility of increased TCF near European Atlantic coast^{34,35}. Here we found an opposite change, but with a fully coupled GCM, larger ensemble members, and an extended and continuous simulation period from past to the end of 21st century.

We also showed that the future ACE near Western Europe may decrease, dominated by the reduction in TCF in that region, with no significant change in TC intensity. It might be surprising to observe a lack of TC intensity change near Western Europe, especially given the relatively high confidence in the increasing fraction of major TCs relative to total TCs globally in the future^{16,36}. However, major TCs often reach their peak intensity in the warm tropics, which is far from Western Europe that we are focusing on in this study. The environmental changes at mid-latitudes may further complicate the understanding of general tropical cyclone intensity changes, which are established based on a tropical environment. In addition, the North Atlantic is a basin where we have very low confidence in the poleward migration of TCF compared to, for example, the western North Pacific^{16,37–39}. Therefore, a reduction in TC-related hazards in Western Europe may be plausible in the future under global warming.

Methods

Data

The TC best track. The TC best track data used in this study was based on the HURDAT best track data⁴⁰ as observational records. Our analysis started in 1966, which is considered the starting year of the geostationary satellite era for North Atlantic hurricane observation. We retained only the best track records from the equator to 60°N. For each TC, we included data from the first time it reached tropical-storm strength (34 kt) to the

last instance it maintained this strength, regardless of its status during the lifecycle, whether it remained a tropical cyclone or underwent an extratropical transition. The TC frequency, TCF, is calculated as the frequency of TC appearances in $5^\circ \times 5^\circ$ grid boxes based on 6-h records. The same data selection criteria and pre-processing were applied to the modeled best track data.

Environmental conditions. We utilized the monthly sea surface temperature (SST) records with 1 deg latitude/longitude grid spacing from the Hadley Centre Sea Ice and Sea Surface Temperature data set⁴¹ known as HadISST. The HadISST data goes back to 1870 but we only used the records for 1966–2020 in this study. For the mean atmospheric conditions, the ERA5 monthly reanalysis data from the European Centre for Medium-Range Weather Forecasts were employed⁴². Based on the seasonality of TCs in the whole North Atlantic basin and near Western Europe (Supplementary Fig. 10), we focused on the environmental conditions during August to October.

Climate indices. The ENSO time series were represented by the oceanic Niño index (ONI). The interdecadal pacific oscillation (IPO) index was estimated as the second principal component of the empirical orthogonal function analysis after standardization for the 13 year filtered global SST²⁷. The Atlantic Multidecadal Oscillation (AMO) was computed as the area weighted average of SST over the North Atlantic with detrending⁴³. The Atlantic Meridional Mode (AMM), describing the meridional variability in the tropical Atlantic Ocean, was calculated based on SST and 10-m wind field^{44–46}.

Large-ensemble simulations

We used the SPEAR global modeling system²³. The version employed here consists of a 50 km-resolution mesh for the atmosphere and land components, and a 1 degree (~100 km) resolution for the sea-ice and ocean components with refinement to 1/3 degree near the Equator^{47–49}. The SPEAR model can simulate the broad-scale distribution of global TCs^{21,23}, but with a limited ability to resolve major TCs. A previously developed TC tracking algorithm⁵⁰ was modified and utilized for TC identification and tracking in the modeling world every 6 h, consistent with the observed best tracks. The TC identification procedure requires a maximum wind speed of 16.5 m s⁻¹ or higher and a well-established warm core defined based on the 300–500-hPa temperature field. The tracking algorithm requires a minimum duration of 36 h. However, the warm-core criterion is not required anymore once a TC is identified and tracked. This means that losing the warm core due to extratropical transition does not terminate a TC lifecycle in the simulated best track, consistent with the observed best track. In this way, the SPEAR model can effectively reproduce the seasonality of TC frequency compared to the observation, both in terms of the global mean value and the TC count near Western Europe (Supplementary Fig. 10).

The initial-condition large-ensemble experiments were conducted with SPEAR. We performed three large-ensemble simulations (AllForc, AllForc_NoAE and NatForc), which are introduced as follows.

AllForc. There are 30 ensemble members in this suite. The simulation period extends from 1966–2014 with historical external forcing, and from 2015–2100 following the Shared Socioeconomic Pathways (SSP2-45 and SSP5-85, respectively). This suite utilized prescribed external forcing including anthropogenic effect (such as greenhouse gases, anthropogenic aerosols, and ozone) and natural forcing (such as volcanic eruptions, dust, and solar constant change). The natural aerosols—e.g., the African dust having a large impact on North Atlantic TC climatology⁵¹—were carefully handled following other previously developed models^{48,49}.

AllForc_NoAE. Like AllForc, but with fixed anthropogenic aerosol forcing, such as sulfates, organic carbon and black carbon, set at the level as in year 1921. There are 12 ensemble members covering 1966–2020. It was shown previously²⁴ that 12 members can effectively remove the climate internal variability by taking the ensemble mean.

NatForc. Like AllForc, but with fixed anthropogenic forcing at the level of 1921. There are 30 ensemble members covering 1966–2100.

We attempted to decompose the impacts of anthropogenic forcing on TCF into anthropogenic GHG forcing and anthropogenic aerosol forcing as follows:

- *Anthropogenic aerosol forcing (1966–2020):* the ensemble-mean TCF trend difference between experiments *AllForc* minus *AllForc_NoAE*.
- *Anthropogenic GHG forcing (1966–2020):* the ensemble-mean TCF trend difference between experiments *AllForc_NoAE* minus *NatForc*.
- *Anthropogenic GHG forcing (2030–2100):* the ensemble-mean TCF trend difference between experiments *AllForc* minus *NatForc*. It has been recently reported that the TCF over North Atlantic has been mainly influenced by the aerosol emission in the US and Europe, which may be substantially flattened out after 2030 owing to pollution control measures over Europe (Supplementary Fig. 3 using sulfate aerosol as an example). This suggests that the difference of simulated TCF trends between *AllForc* and *NatForc* for 2030–2100 should be mainly due to the anthropogenic GHG forcing.

SVD analysis

The singular value decomposition (SVD) was used here to explore the synchronized temporal and spatial relationship between observed SST and TCF matrixes. For each SVD mode, a pair of expansion coefficient (EC) time series were generated for SST and TCF. To show the fraction of co-

variability between the SST and TCF patterns in each mode, a squared covariance fraction (SFC) was calculated in a unit of percentage.

Following a recent study²⁴, global and regional SVD approaches were employed. Both approaches utilize the global SST field as one input. For the other input matrix, the global SVD utilizes basin-wide TCF, whereas the TCF information on one and its eight neighboring grids are used for one regional SVD practice. The regional SVD is repeated until all the grids in the North Atlantic basin is covered. In our analysis, most of regional SVD result in two leading modes corresponding to global warming and IPO based on the SFC ranking.

The global SVD was employed in Supplementary Fig. 2, with the regional SVD in Fig. 1. The SST and TCF fields were weighted by the cosine of latitude before performing the matrix analysis.

Decomposition of TCF trends

We utilized two previously developed empirical methods⁵² to break down the TCF trends into genesis and/or track contributions.

The first empirical approach is the *Total Analysis*. The results of the Total Analysis are shown in Table 1 and Supplementary Fig. 4.

The TCF in an individual grid *A* can be written as

$$\bar{f} = \iint_C \bar{g} \times \bar{t} dA_o \tag{1}$$

where $\bar{f} = f(A)$ is the TCF in an individual grid *A*, $g = g(A_o)$ is the frequency of TC genesis in a remote grid cell A_o , $t = t(A, A_o)$ is the probability that a TC is generated in the grid A_o and then propagated to grid *A* (i.e., track effect), and *C* is the region over which the integration is calculated. The overbars represent the climatological means.

Now we decompose *f* in 1 year with the climatological mean (\bar{f}) and the anomaly (f') in this year, i.e., $f = \bar{f} + f'$, and Eq. (1) can be then rewritten as

$$\bar{f} + f' = \iint_C (\bar{g} + g') \times (\bar{t} + t') dA_o \tag{2}$$

where \bar{g} and \bar{t} are the climatological means and g' and t' are the anomalies in that year. Substituting Eq. (1) in Eq. (2) yields

$$f' = \iint_C g' \times \bar{t} dA_o + \iint_C \bar{g} \times t' dA_o + \iint_C g' \times t' dA_o \tag{3}$$

The map of TCF trend, denoted as $\frac{\partial}{\partial t}(\bar{f} + f') = \frac{\partial}{\partial t} f'$, can be then decomposed with Eq. (3) as

$$\frac{\partial}{\partial t} f' = \frac{\partial}{\partial t} \left(\iint_C g' \times \bar{t} dA_o \right) + \frac{\partial}{\partial t} \left(\iint_C \bar{g} \times t' dA_o \right) + \frac{\partial}{\partial t} \left(\iint_C g' \times t' dA_o \right). \tag{4}$$

Next we apply Eq. (4) to experiment 1, a reference experiment, which can be written as

$$\frac{\partial}{\partial t} f'_1 = \frac{\partial}{\partial t} \left(\iint_C g'_1 \times \bar{t}_1 dA_o \right) + \frac{\partial}{\partial t} \left(\iint_C \bar{g}_1 \times t'_1 dA_o \right) + \frac{\partial}{\partial t} \left(\iint_C g'_1 \times t'_1 dA_o \right). \tag{5}$$

We may also apply Eq. (4) to experiment 2, a sensitivity experiment, which can be written as

$$\frac{\partial}{\partial t} f'_2 = \frac{\partial}{\partial t} \left(\iint_C g'_2 \times (\bar{t}_1 + \Delta \bar{t}) dA_o \right) + \frac{\partial}{\partial t} \left(\iint_C (\bar{g}_1 + \Delta \bar{g}) \times t'_2 dA_o \right) + \frac{\partial}{\partial t} \left(\iint_C g'_2 \times t'_2 dA_o \right), \tag{6}$$

where $\Delta \bar{t} = \bar{t}_2 - \bar{t}_1$ and $\Delta \bar{g} = \bar{g}_2 - \bar{g}_1$, which represent the difference of climatological mean of track probability and genesis frequency, respectively, in experiment 2 relative to experiment 1.

By taking the difference of Eqs. (6) and (5) we have

$$\begin{aligned} \underbrace{\frac{\partial}{\partial t} f'_2 - \frac{\partial}{\partial t} f'_1}_{df} &= \underbrace{\frac{\partial}{\partial t} \left(\iint_C g'_2 \times \bar{t}_1 dA_o \right) - \frac{\partial}{\partial t} \left(\iint_C g'_1 \times \bar{t}_1 dA_o \right)}_{dg} \\ &+ \underbrace{\frac{\partial}{\partial t} \left(\iint_C \bar{g}_1 \times t'_2 dA_o \right) - \frac{\partial}{\partial t} \left(\iint_C \bar{g}_1 \times t'_1 dA_o \right)}_{dt} \\ &+ \underbrace{\frac{\partial}{\partial t} \left(\iint_C g'_2 \times t'_2 dA_o \right) - \frac{\partial}{\partial t} \left(\iint_C g'_1 \times t'_1 dA_o \right)}_{dn} + \frac{\partial}{\partial t} \left(\iint_C g'_2 \times \bar{\Delta t} dA_o \right) + \frac{\partial}{\partial t} \left(\iint_C \bar{\Delta g} \times t'_2 dA_o \right), \end{aligned} \tag{7}$$

where df shows the TCF trend difference between experiments 2 and 1, and dg , dt and dn represent changes due to genesis effect, track effect, and nonlinear combination of the two.

The second empirical approach is the *Origin Analysis*. The result of the Origin Analysis is shown in Supplementary Fig. 5.

The Origin Analysis for TCF trend has been recently derived and employed in another study²⁴. Here we only briefly introduce this method, which can be conveniently written as

$$df_{B,A_o} = dg_{B,A_o} + dt_{B,A_o} + dn_{B,A_o} \tag{8}$$

where df_{B,A_o} shows the total genesis and track effects of a remote genesis grid A_o on the TCF trend difference between the two experiments in the region of B (referring to the magenta box near Western Europe in Fig. 1a in this study). The three terms on the r.h.s., dg_{B,A_o} , dt_{B,A_o} and dn_{B,A_o} , show the breakdown effects of genesis, track, and nonlinear combination of the two, respectively, from a remote genesis grid A_o on the mean TCF change in the region of B .

The total analysis reveals the contribution of each of the three factors—genesis effect, track effect, and their nonlinear combination as shown in Eq. (7)—to the change in TCF across the entire domain. However, the total analysis cannot pinpoint the specific locations where these changes significantly impact local TCF. Conversely, the origin analysis, described in Eq. (8), identifies the specific locations contributing to the projected change in TCF near Western Europe.

Genesis Potential Index (GPI)

Two kinds of GPI were utilized in this study: the ENGPI²⁸ and DGPI⁵³. The DGPI is composed with dynamical environmental factors, which can be written as

$$\begin{aligned} DGPI &= \underbrace{(2.0 + 0.1 \times V_s)^{-1.7}}_{V-SHEAR} \underbrace{\left(5.5 - \frac{du_{500}}{dy} \times 10^5 \right)^{2.3}}_{M-SHEAR} \\ &\underbrace{(5.0 - 20 \times \omega_{500})^{3.4}}_{OMEGA} \underbrace{\left(5.5 + |\zeta_{a850} \times 10^5| \right)^{2.4} e^{-11.8}}_{VORT} - 1.0 \end{aligned} \tag{9}$$

where V_s is the vertical wind shear magnitude ($m s^{-1}$) between 200 and 850 hPa, u_{500} is the zonal wind ($m s^{-1}$) at 500 hPa, $\left(-\frac{du_{500}}{dy} \right)$ denotes the meridional shear vorticity (s^{-1}) at 500 hPa, ω_{500} is the vertical velocity in a pressure coordinate ($Pa s^{-1}$), ζ_{a850} is the absolute vorticity (s^{-1}) at 850 hPa, and e is the natural base. The calculated DGPI value was fixed to zero between 5°N–5°S or where the relative SST (i.e., local SST minus tropical mean SST) becomes negative^{29,53}.

We took the logarithm of Eq. (9) to estimate the relative contribution of each term to the change of DPGI, which can be written as

$$\begin{aligned} \log(DGPI + 1) &= \log(V - SHEAR) + \log(M - SHEAR) \\ &+ \log(OMEGA) + \log(VORT) - 11.8 \end{aligned} \tag{10}$$

The linear trend of each in Eq. (10) was compared to obtain the relative contribution of individual environmental factors to the total DPGI trend, as given in Table 2.

The ENGPI is defined as²⁸

$$ENGPI = |10^5 \zeta_{a850}|^{\frac{3}{2}} \left(\frac{RH}{50} \right)^3 \left(\frac{V_{pot}}{70} \right)^3 (1 + 0.1V_s)^{-2} \tag{11}$$

where V_{pot} is the maximum potential intensity ($m s^{-1}$) defined by the local thermodynamic profile⁵⁴, and RH denotes the relative humidity (%) at 600 hPa.

Statistical significance test

We assessed the statistical significance between two linear trends using a t -test. For the epochal TCF change (e.g., in Fig. 1a), a bootstrap method was applied. We resampled the two tested populations in pairs 10,000 times, calculated the mean difference for each pair, and generated a new distribution with 10,000 samples. From this distribution, we derived the 90% confidence intervals.

Data availability

The HURDAT best track data was taken as a subset of the IBTrACS dataset that can be downloaded from the National Centers for Environmental Information website (<https://www.ncei.noaa.gov/data/international-best-track-archive-for-climate-stewardship-ibtracs/v04r00/access/csv/ibtracs.ALL.list.v04r00.csv>). The ERA5 monthly reanalysis data was downloaded from The Copernicus Climate Change Service (<https://cds.climate.copernicus.eu/cdsapp#!/dataset/reanalysis-era5-pressure-levels-monthly-means?tab=overview>). The HadISST data was accessed via the UK Met Office Hadley Centre (https://www.metoffice.gov.uk/hadobs/hadisst/data/HadISST_sst.nc.gz). The SPEAR large-ensemble data for the AllForc experiments are online available at <https://noaa-gfdl-spear-large-ensembles-pds.s3.amazonaws.com/index.html#SPEAR/GFDL-LARGE-ENSEMBLES/CMIP/NOAA-GFDL/GFDL-SPEAR-MED/>.

Code availability

The source codes for the analysis of this study are available from the corresponding author upon reasonable request.

Received: 11 March 2024; Accepted: 15 July 2024;

Published online: 23 July 2024

References

- Rantanen, M., Räisänen, J., Sinclair, V. A. & Lento, J. The extratropical transition of Hurricane Ophelia (2017) as diagnosed with a generalized omega equation and vorticity equation. *Tellus A Dyn. Meteorol. Oceanogr.* **72**, 1721215 (2020).
- Laurila, T. K., Sinclair, V. A. & Gregow, H. The extratropical transition of Hurricane Debby (1982) and the subsequent development of an intense windstorm over Finland. *Mon. Weather Rev.* **148**, 377–401 (2020).

3. Grams, C. M. & Blumer, S. R. European high-impact weather caused by the downstream response to the extratropical transition of North Atlantic hurricane Katia (2011). *Geophys. Res. Lett.* **42**, 8738–8748 (2015).
4. Graham, E. & Smart, D. ‘Hurricane’ Debbie—60 years on: a fresh analysis. *Weather* **76**, 284–292 (2021).
5. Baker, A. J., Hodges, K. I., Schiemann, R. K. H. & Vidale, P. L. Historical variability and lifecycles of north Atlantic midlatitude cyclones originating in the tropics. *J. Geophys. Res. Atmos.* **126**, e2020JD033924 (2021).
6. Dekker, M. M., Haarsma, R. J., Vries, H., de Baatsen, M. & Delden, A. Characteristics and development of European cyclones with tropical origin in reanalysis data. *Clim. Dyn.* **50**, 445–455 (2018). J. va.
7. Hart, R. E. & Evans, J. L. A climatology of the extratropical transition of Atlantic tropical cyclones. *J. Clim.* **14**, 546–564 (2001).
8. Evans, C. et al. The extratropical transition of tropical cyclones. Part I: Cyclone evolution and direct impacts. *Mon. Weather Rev.* **145**, 4317–4344 (2017).
9. Jones, S. C. et al. The extratropical transition of tropical cyclones: forecast challenges, current understanding, and future directions. *Weather Forecast* **18**, 1052–1092 (2003).
10. Amott, J. M. & Evans, J. L. Characterization of extratropical transition using cluster analysis. *Bull. Am. Meteorol. Soc.* **132**, 2127–2131 (2004).
11. Kofron, D. E., Ritchie, E. A. & Tyo, J. S. Determination of a consistent time for the extratropical transition of tropical cyclones. Part II: potential vorticity metrics. *Mon. Weather Rev.* **138**, 4344–4361 (2010).
12. Sainsbury, E. M. et al. How important are post-tropical cyclones for European windstorm risk? *Geophys. Res. Lett.* **47**, e2020GL089853 (2020).
13. Woodruff, J. D., Irish, J. L. & Camargo, S. J. Coastal flooding by tropical cyclones and sea-level rise. *Nature* **504**, 44–52 (2013).
14. Walsh, K. J. E. et al. Tropical cyclones and climate change. *Wiley Interdiscip. Rev. Clim. Chang.* **7**, 65–89 (2016).
15. Knutson, T. et al. Tropical cyclones and climate change assessment: part I: detection and attribution. *Bull. Am. Meteorol. Soc.* **100**, 1987–2007 (2019).
16. Knutson, T. et al. Tropical cyclones and climate change assessment: part II: projected response to anthropogenic warming. *Bull. Am. Meteorol. Soc.* **101**, E303–E322 (2020).
17. Sobel, A. H. et al. Tropical cyclone frequency. *Earth's Futur.* **9**, e2021EF002275 (2021).
18. Wallace, E. J. & Dee, S. G. Tropical cyclone frequency: turning paleoclimate into projections. *Environ. Res. Clim.* **1**, 023002 (2022).
19. Daloz, A. S. et al. Cluster analysis of downscaled and explicitly simulated North Atlantic tropical cyclone tracks. *J. Clim.* **28**, 1333–1361 (2015).
20. Vecchi, G. A. et al. Tropical cyclone sensitivities to CO₂ doubling: roles of atmospheric resolution, synoptic variability and background climate changes. *Clim. Dyn.* **53**, 5999–6033 (2019).
21. Murakami, H. et al. Detected climatic change in global distribution of tropical cyclones. *Proc. Natl Acad. Sci. USA* **117**, 10706–10714 (2020).
22. Murakami, H. Substantial global influence of anthropogenic aerosols on tropical cyclones over the past 40 years. *Sci. Adv.* **8**, 1–11 (2022).
23. Delworth, T. L. et al. SPEAR: the next generation GFDL modeling system for seasonal to multidecadal prediction and projection. *J. Adv. Model. Earth Syst.* **12**, 1–36 (2020).
24. Wang, S., Murakami, H. & Cooke, W. F. Anthropogenic forcing changes coastal tropical cyclone frequency. *npj Clim. Atmos. Sci.* **6**, 187 (2023).
25. Landsea, C. W., Vecchi, G. A., Bengtsson, L. & Knutson, T. R. Impact of duration thresholds on Atlantic tropical cyclone counts. *J. Clim.* **23**, 2508–2519 (2010).
26. Henley, B. J. et al. A triple index for the interdecadal Pacific oscillation. *Clim. Dyn.* **45**, 3077–3090 (2015).
27. Folland, C. K. Relative influences of the interdecadal Pacific oscillation and ENSO on the South Pacific convergence zone. *Geophys. Res. Lett.* **29**, 1643 (2002).
28. Emanuel, K. A. & Nolan, D. S. *Tropical Cyclone Activity and the Global Climate System*. In *Proc. of 26th Conf. on Hurricanes and Tropical Meteorology*. 240–241 (American Meteorological Society, Miami, FL, 2004).
29. Wang, B. & Murakami, H. Dynamic genesis potential index for diagnosing present-day and future global tropical cyclone genesis. *Environ. Res. Lett.* **15**, 114008 (2020).
30. Allen, R. J., Sherwood, S. C., Norris, J. R. & Zender, C. S. The equilibrium response to idealized thermal forcings in a comprehensive GCM: implications for recent tropical expansion. *Atmos. Chem. Phys.* **12**, 4795–4816 (2012).
31. Fu, Q., Johanson, C. M., Wallace, J. M. & Reichler, T. Enhanced mid-latitude tropospheric warming in satellite measurements. *Science* **312**, 1179–1179 (2006).
32. Bell, G. D. et al. Climate assessment for 1999. *Bull. Am. Meteorol. Soc.* **81**, s1–s50 (2000).
33. Stansfield, A. M., Reed, K. A. & Zarzycki, C. M. Changes in precipitation from North Atlantic tropical cyclones under RCP scenarios in the variable-resolution community atmosphere model. *Geophys. Res. Lett.* **47**, 1–10 (2020).
34. Haarsma, R. J. et al. More hurricanes to hit western Europe due to global warming. *Geophys. Res. Lett.* **40**, 1783–1788 (2013).
35. Baatsen, M., Haarsma, R. J., Van Delden, A. J. & de Vries, H. Severe autumn storms in future western Europe with a warmer Atlantic ocean. *Clim. Dyn.* **45**, 949–964 (2015).
36. Kossin, J. P., Knapp, K. R., Olander, T. L. & Velden, C. S. Global increase in major tropical cyclone exceedance probability over the past four decades. *Proc. Natl Acad. Sci. USA* **117**, 11975–11980 (2020).
37. Kossin, J. P., Emanuel, K. A. & Vecchi, G. A. The poleward migration of the location of tropical cyclone maximum intensity. *Nature* **509**, 349–352 (2014).
38. Kossin, J. P., Emanuel, K. A. & Camargo, S. J. Past and projected changes in western north Pacific tropical cyclone exposure. *J. Clim.* **29**, 5725–5739 (2016).
39. Wang, S. & Toumi, R. Recent migration of tropical cyclones toward coasts. *Science* **371**, 514–517 (2021).
40. Landsea, C. W. & Franklin, J. L. Atlantic hurricane database uncertainty and presentation of a new database format. *Mon. Weather Rev.* **141**, 3576–3592 (2013).
41. Rayner, N. A. et al. Global analyses of sea surface temperature, sea ice, and night marine air temperature since the late nineteenth century. *J. Geophys. Res.* **108**, 4407 (2003).
42. Hersbach, H. et al. The ERA5 global reanalysis. *Q. J. R. Meteorol. Soc.* **146**, 1999–2049 (2020).
43. Enfield, D. B., Mestas-Nuñez, A. M. & Trimble, P. J. The Atlantic multidecadal oscillation and its relation to rainfall and river flows in the continental U.S. *Geophys. Res. Lett.* **28**, 2077–2080 (2001).
44. Kossin, J. P. & Vimont, D. J. A more general framework for understanding Atlantic hurricane variability and trends. *Bull. Am. Meteorol. Soc.* **88**, 1767–1782 (2007).
45. Vimont, D. J. & Kossin, J. P. The Atlantic meridional mode and hurricane activity. *Geophys. Res. Lett.* **34**, 1–5 (2007).
46. Chiang, J. C. H. & Vimont, D. J. Analogous Pacific and Atlantic meridional modes of tropical atmosphere–ocean variability*. *J. Clim.* **17**, 4143–4158 (2004).
47. Adcroft, A. et al. The GFDL global ocean and sea ice model OM4.0: model description and simulation features. *J. Adv. Model. Earth Syst.* **11**, 3167–3211 (2019).
48. Zhao, M. et al. The GFDL global atmosphere and land model AM4.0/LM4.0: 1 simulation characteristics with prescribed SSTs. *J. Adv. Model. Earth Syst.* **10**, 691–734 (2018).

49. Zhao, M. et al. The GFDL global atmosphere and land model AM4.0/LM4.0: 2. model description, sensitivity studies, and tuning strategies. *J. Adv. Model. Earth Syst.* **10**, 735–769 (2018).
50. Harris, L. M., Lin, S.-J. & Tu, C. High-resolution climate simulations using GFDL HiRAM with a stretched global grid. *J. Clim.* **29**, 4293–4314 (2016).
51. Reed, K. A. et al. Exploring the impact of dust on north Atlantic hurricanes in a high-resolution climate model. *Geophys. Res. Lett.* **46**, 1105–1112 (2019).
52. Murakami, H., Wang, B., Li, T. & Kitoh, A. Projected increase in tropical cyclones near Hawaii. *Nat. Clim. Chang.* **3**, 749–754 (2013).
53. Murakami, H. & Wang, B. Patterns and frequency of projected future tropical cyclone genesis are governed by dynamic effects. *Commun. Earth Environ.* **3**, 77 (2022).
54. Emanuel, K. Sensitivity of tropical cyclones to surface exchange coefficients and a revised steady-state model incorporating eye dynamics. *J. Atmos. Sci.* **52**, 3969–3976 (1995).

Acknowledgements

This report was prepared by Shuai Wang under award NA18OAR4320123 from the National Oceanic and Atmospheric Administration, U.S. Department of Commerce. The statements, findings, conclusions, and recommendations are those of the author(s) and do not necessarily reflect the views of the National Oceanic and Atmospheric Administration, or the U.S. Department of Commerce. Shuai Wang was also partly funded by the Singapore Green Finance Centre.

Author contributions

S.W. and H.M. conceived the study. W.C. conducted model simulations. S.W. performed the analysis and wrote the initial draft of the paper. H.M. made suggestions that helped to improve the initial manuscript. All authors made contributions for further improvement of the manuscript.

Competing interests

The authors declare no competing interests.

Additional information

Supplementary information The online version contains supplementary material available at <https://doi.org/10.1038/s41612-024-00721-2>.

Correspondence and requests for materials should be addressed to Shuai Wang.

Reprints and permissions information is available at <http://www.nature.com/reprints>

Publisher's note Springer Nature remains neutral with regard to jurisdictional claims in published maps and institutional affiliations.

Open Access This article is licensed under a Creative Commons Attribution 4.0 International License, which permits use, sharing, adaptation, distribution and reproduction in any medium or format, as long as you give appropriate credit to the original author(s) and the source, provide a link to the Creative Commons licence, and indicate if changes were made. The images or other third party material in this article are included in the article's Creative Commons licence, unless indicated otherwise in a credit line to the material. If material is not included in the article's Creative Commons licence and your intended use is not permitted by statutory regulation or exceeds the permitted use, you will need to obtain permission directly from the copyright holder. To view a copy of this licence, visit <http://creativecommons.org/licenses/by/4.0/>.

© The Author(s) 2024